molecules

MDPI

Article

Tungsten and Molybdenum Heteropolyanions with Different Central Ions—Correlation between Theory and Experiment

Piotr Niemiec [1,*], Renata Tokarz-Sobieraj [2,*] and Małgorzata Witko [2]

[1] Faculty of Mathematics and Natural Sciences, Department of Chemistry, University of Applied Sciences in Tarnow, Mickiewicza 8, 33-100 Tarnow, Poland
[2] Jerzy Haber Institute of Catalysis and Surface Chemistry, Polish Academy of Sciences, Niezapominajek 8, 30-239 Krakow, Poland; malgorzata.witko@ikifp.edu.pl
* Correspondence: p_niemiec@pwsztar.edu.pl (P.N.); renata.tokarz-sobieraj@ikifp.edu.pl (R.T.-S.); Tel.: +48-12-6395152 (R.T.-S.)

Abstract: Density functional theory calculations were carried out to investigate the electronic structures of Keggin-typed $[XMo_{12}O_{40}]^{n-}$ and $[XW_{12}O_{40}]^{n-}$ anions with different heteroatoms (X = Zn^{2+}, B^{3+}, Al^{3+}, Ga^{3+}, Si^{4+}, Ge^{4+}, P^{5+}, As^{5+}, and S^{6+}). The influence of solvent on redox properties of heteropolyanions was discussed. For $[XW_{12}O_{40}]^{n-}$ systems two linear correlation: first, between the experimental redox potential and energies of LUMO orbital; and second, between the experimental redox potential and total energy interaction (calculated between internal tetrahedron (XO_4^{n-}), and rest of Kegging anion skeleton, ($W_{12}O_{36}$)) were designated. Taking into account the similarity of $XW_{12}O_{40}^{n-}$ and $XMo_{12}O_{40}^{n-}$ systems (in geometry and electronic structure), the estimated redox potential of molybdenum heteropolyanions (with X being p block elements) in different solvent were proposed.

Keywords: heteropolyacids; DFT calculations; correlations analysis; redox potential; energy decomposition analysis (EDA)

Citation: Niemiec, P.; Tokarz-Sobieraj, R.; Witko, M. Tungsten and Molybdenum Heteropolyanions with Different Central Ions—Correlation between Theory and Experiment. *Molecules* **2022**, *27*, 187. https://doi.org/10.3390/molecules27010187

Academic Editor: Giorgio Vilardi

Received: 9 December 2021
Accepted: 23 December 2021
Published: 29 December 2021

1. Introduction

Heteropolyacid (HPA) systems belong to a group of compounds, which due to their acid–base and redox properties, are used in numerous catalytic processes both homogeneous and heterogeneous [1–16]. They have several advantages as catalysts, which make them economically and environmentally attractive; the most meaningful are their versatility (in the sense of electronic and geometry structure as well as chemical composition), performance in moderate reaction conditions, thermal stability and stability in solutions, simple recovery, and recycling. HPA catalysts are currently used in several industrial processes including selective oxidation of ethene/methacrolein, hydration of propene/buthene, polymerization of tetrahydrofuran and coupling reactions [3].

The important parameter that makes HPAs useful in catalysis is their reduction potential (oxidizing power) measuring of tendency of chemical species to acquire electrons, and thereby become reduced. Several theoretical and experimental methods were employed to determine that parameter. The reduction potential of HPA can be established by the measuring of absorption edge positions in the UV–Vis spectra [17] or negative differential resistance (NDR) peak voltages in scanning tunneling microscope STM [17–22], but the most conventional technique is the electrochemical method. Redox potential obtained by electrochemical measuring depends on composition of electrolyte solution (pH), the identity of the electrodes and other parameters (for example, measurement conditions). As a result, there is little experimental data obtained in the same condition for various solvent and different HPA [23–25]. Although, there are some exceptions including: redox potential for $H_nXMo_{12}O_{40}$ (where: X = P, As, Si, Ge) [26], for $H_nXW_{12}O_{40}$ (where X = P, Si, Co, Fe, B) [23,25,27–29], modified molybdenum and tungsten heteropolyacids with P^{5+}/Si^{4+} as central ion in various solvents, such as H_2SO_4 [30], $HClO_4$ [31], CH_3CN [32],

and Na_2SO_4 [33]. In all of the abovementioned papers/cases, the correlation between one-electron redox potential and global ionic charge of heteropolyacids systems were reported.

Several theoretical methods were employed to determine the theoretical description of redox potential in HPA systems [26,34–38]. This matter was addressed mainly by Poblet group [34–37] who studied the $XM_{12}O_{40}^{n-}$ and $SiM_{11}VO_{40}^{5-}$ systems (M = W^{6+}, Mo^{6+}, X = Al^{3+}, Si^{4+}, P^{5+}, Fe^{3+}, Co^{3+}, and Co^{2+}) and demonstrated that the introduction of additional electron to the system results in its delocalization onto all twelve polyatoms and formation of reduced "blue species." An attempt to systematize the assessment of the oxidation and reduction abilities of heteropolyanions was undertaken in [35,36] through analysis of the so-called anion charge effect. It was shown that by defining the molecular charge density q/m (q = total charge of heteropolyanion, m = number of equivalent metal centers) the results can be generalized to all polyoxometalates. This conclusion was confirmed by Pope in 1983 [36], who assumed that the reduction potential changes by -0.18 V per each unit of the total heteropolyanion charge with the Keggin structure. The influence of the size of the central ion on the redox properties of HPAs systems was examined in [38] where it was demonstrated that the chemical nature of central ion determines the electrostatic potential of the internal tetrahedron, affecting the metal and oxygen skeleton. Central units with a greater negative charge (e.g., -6, XO_4^{n-}) achieve more negative potential in the metal–oxygen environment $W_{12}O_{36}$, which reduces the system's tendency to receive electrons, lowering the redox potential. Attempts to correlate redox properties with the atomic radius of the central ion (the size of the internal tetrahedron) evidence that the smaller the tetrahedron size and the larger its charge, the greater impact on the metal–oxygen skeleton. Another factor that affects redox property of HPA system is its geometric structure [34]. Based on DFT calculations carried out for the five geometric isomers of the Keggin anion it was found that the mutual arrangement of triplet units determines the energy of unoccupied frontier orbitals affecting oxidation and reduction abilities of the systems that change in order: $\alpha > \beta > \gamma > \delta > \varepsilon$.

For a long time, HPA science was concentrated mainly around designing and synthesizing structures but for some time it is gravitating towards the examination of more interdisciplinary multifunctional materials and related areas to diversify future possibilities of POMs (Polyoxometalates) [38,39]. Thanks to the attractive topologies and exceptional properties explored in gas adsorption and separation, heterogeneous catalysis, ion exchange, chiral resolution, magnetism, luminescence, and nonlinear optical properties POM scientists have taken up a challenge to introduce POMs into Coordination Polymer systems (CP) building POMCPs. CPs are built from metal ions or metal clusters and organic ligands unit joined together via coordination bonds (or even supramolecular interactions); they present a highly ordered structure with repeating coordination entities extending in one, two, or three dimensions [40]. Keggin-type POMs, can be treated as one of the best candidates for designing functional POMCPs. Furthermore, POMCPs based on Keggin-type unit represent over 50% of the described members of this family [41,42]. In addition, one should stress that POMCPs present a lot of different and attractive applications in: photocatalysis [43–59], electrocatalysis [60–68], magnetism [69–74], and photoluminescence [75–83].

The main goal of this work is to find the correlation between redox potentials and calculated parameters describing the electronic structure of modified HPA by discussing the impact of various central ions on the electronic structure of $[XMo_{12}O_{40}]^{n-}$ and $[XW_{12}O_{40}]^{n-}$ Keggin anions.

2. Results and Discussion

From the literature data it is known that redox potential of heteropolyacids systems depend on the global charge of the heteropolyanion; there is no further information about differences between systems with various central ions having the same global charge. Therefore, we decided to analyze and find parameters, which not only determine the electronic structure of HPA systems with various central anion, but also can be compared with experimental data.

2.1. $XW_{12}O_{40}^{n-}$ Systems

The available literature data suggest that the search for a quantitative correlation between the experimental results and the calculated theoretical parameters should be primarily focused on the analysis of boundary orbitals. Therefore Table 1 summarizes the energy of frontier orbitals (HOMO, LUMO) and the size of the band gap, for $XW_{12}O_{40}^{n-}$ systems for calculations made in vacuum and in solvents: acetonitrile and water as generally used in the reaction with heteropolyacids systems. The presented results show the large differences for systems under vacuum and in solution. In a vacuum, energies of frontier orbitals for various systems strongly depend on X belonging to particular groups in the periodic table. The differences in values of energy of frontier orbitals between groups can be as high as 2–3 eV (e.g., energy of LUMO orbital in vacuum: Zn^{2+} 10.52; B^{3+} 7.99; Si^{4+} 5.17). Much smaller differences are observed for the systems tested in solvents. Here on going from group to group, energies of HOMO/LUMO orbitals changes about 0.3 eV (e.g., energy of LUMO orbital in water: Zn^{2+} −3.55; B^{3+} −3.77; Si^{4+} −4.14). Within group (for cations with the same valence charge) the energies values of frontier orbitals are much smaller (e.g., energy of HOMO orbital in water: Si^{4+} −6.74; Ge^{4+} −6.73).

Table 1. Energies of frontier (HOMO, LUMO) orbitals, E_{HOMO} and E_{LUMO} (eV) and the band gap for $XW_{12}O_{40}^{n-}$ systems in vacuum, water and acetonitrile-CH_3CN (top, middle, and bottom part of the table, respectively). Additionally total energy, ΔE_{int} (a.u.), and experimental redox potential E_{red} (V) for $XW_{12}O_{40}^{n-}$ system in acetonitrile, are presented (the last two rows).

X	Zn^{2+}	B^{3+}	Al^{3+}	Ga^{3+}	Si^{4+}	Ge^{4+}	P^{5+}	As^{5+}	S^{6+}
					Vacuum				
E_{HOMO}	8.23	5.99	5.29	5.28	2.59	2.57	−0.15	−0.16	−2.89
E_{LUMO}	10.52	7.99	7.87	7.84	5.17	5.13	2.41	2.37	−0.38
Gap	2.29	2.00	2.58	2.56	2.58	2.56	2.56	2.53	2.51
					Water (H_2O)				
E_{HOMO}	−5.78	−5.71	−6.43	−6.43	−6.74	−6.73	−7.04	−7.03	−7.33
E_{LUMO}	−3.55	−3.77	−3.83	−3.84	−4.14	−4.16	−4.47	−4.49	−4.81
Gap	2.23	1.94	2.60	2.59	2.60	2.57	2.57	2.54	2.52
					Acetonitrile (CH_3CN)				
E_{HOMO}	−5.50	−5.48	−6.20	−6.19	−6.55	−6.55	−6.89	−6.90	−7.24
E_{LUMO}	−3.26	−3.53	−3.59	−3.61	−3.95	−3.97	−4.33	−4.36	−4.72
Gap	2.24	1.95	2.61	2.58	2.60	2.58	2.56	2.54	2.52
ΔE_{int} [a.u.]	−1.122	−0.907	−0.808	−0.804	−0.570	−0.571	−0.345	−0.348	−0.145
E_{red} [eV]	−1.92	−1.65	−1.56	−1.54	−1.13	−1.09	−0.64	−0.67	−0.26

ΔE_{int}—total energy interaction between the internal tetrahedron (XO_4^{n-}) and the metal–oxygen framework ($W_{12}O_{36}$). E_{red}—experimentally [84] obtained redox potential.

The theoretical parameters calculated for anions system in acetonitrile such as the energy of the HOMO or LUMO orbitals and the size of the energy gap are confronted against redox potential, obtained experimentally by K. Nakijima [84] through performing cyclic voltamperometry measurements (water content below <50 ppm). Only the correlation of the LUMO energy with the redox potential values is linear. The results presented in Figure 1 shows the linear correlation (R^2 = 0.999) between calculated energy of LUMO orbital, E_{LUMO}, and experimental values of the redox potential E_{red}. From correlation it is evident that increase in LUMO energy causes decreases in redox potential, and as a result, oxidizing power of heteropolyanion weakens. Based on LUMO energy levels for two boundary systems, with the highest ($ZnW_{12}O_{40}^{6-}$) and the lowest anion charge ($SW_{12}O_{40}^{2-}$), −3.26 eV and −4.72 eV, respectively, one can indicate the $SW_{12}O_{40}^{2-}$ system as exhibiting the highest oxidizing power, whereas $ZnW_{12}O_{40}^{2-}$ as showing the lowest one.

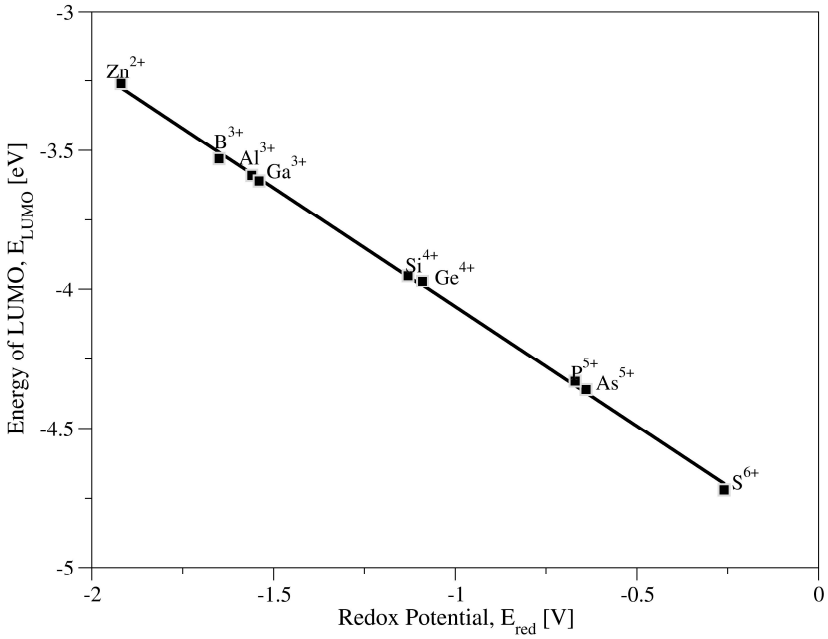

Figure 1. Correlation between energy of LUMO (Lowest Unoccupied Molecular Orbitals), E_{LUMO} (eV), and experimentally obtained [84] redox potential, E_{red} (V), for $XW_{12}O_{40}{}^{n-}$ in CH_3CN as a solution.

The correlations found for the studied systems call for a much closer analysis of the frontier orbitals. Table 2 shows the percentage composition of HOMO, LUMO orbitals of $[XW_{12}O_{40}]^{n-}$ where X = Zn^{2+}, B^{3+}, Al^{3+}, Ga^{3+}, Si^{4+}, Ge^{4+}, P^{5+}, As^{5+}, and S^{6+}. HOMO orbitals of the studied systems are almost identical except systems with B^{3+} and Zn^{2+} as the central ions whereas energies differ significantly. In all cases HOMO are composed of the *2p* orbitals of bridging oxygens (double-coordinated to two addenda atoms) Ob (43–47%) and Oc (50–52%). As previously noted, the exception is the system with B^{3+}, in the position of the central ion, where HOMO is built of *2p* orbitals of internal, Oa, oxygen atoms, (∼77%), coordinated with the central ion and one addenda and *2p* orbitals of terminal oxygen ions Od (∼10%), individually coordinated with tungsten atoms. In case of second exception ZnW system, the orbital is composed of *3d* central ion, Zn^{2+} as well as of *2p* orbitals of oxygen ions from the internal tetrahedral Oa (∼51%) and orbitals of bridging oxygen ions Oc (∼26%) with admixture of *2p* Zn orbitals. Unlike the HOMO orbitals, the composition of the LUMO orbitals is identical for all calculated systems. Their consist of *5d* orbitals of addenda atoms W (∼75%) with small amount of *2p* orbitals of bridging oxygen centers Ob (∼12%) and Oc (∼13%).

The received, almost identical, compositions of frontier orbitals do not explain neither the differences in the energy of the frontier orbitals nor differences in redox potential of the systems observed in the experiment. Therefore, the discussion was extended to the analysis of the valence band and the conduction band near the Fermi level. Figure 2 shows an example of the spectrum of electron density for the reference PW system. Analysis of various parts of the valence band and conduction band shows that in the valence band, in the immediate vicinity of the gap (located between the valence band and the conduction band) the bridging oxygens of Ob and Oc prevail, while in the area with slightly lower energy, the Od terminal oxygen ions dominate, next to which, there are also orbitals of internal oxygen ions Oa. In the central part of the valence band there are *2p* orbitals of mostly bridging and terminal oxygen ions with the insignificant amount of *5d* tungsten orbitals. The conduction band is built mainly of *5d* tungsten orbitals with a small amount of *2p* orbitals of bridging oxygen ions.

Table 2. Decomposition into atomic contribution (in %) of HOMO and LUMO orbitals in $XW_{12}O_{40}^{n-}$ system.

X	B^{3+}	Al^{3+}	Si^{4+}	P^{5+}	S^{6+}	Zn^{2+}	Ga^{3+}	Ge^{4+}	As^{5+}
					HOMO				
X	0.00	0.01	0.00	0.00	0.00	12.25	0.02	0.00	0.00
Oa	**77.43**	0.39	0.03	0.01	0.01	**50.56**	0.93	0.09	0.02
W	4.16	0.61	0.70	0.84	1.05	2.04	0.64	0.74	0.88
Ob	1.67	**44.78**	**46.47**	**47.26**	**47.71**	2.21	**43.81**	**46.03**	**46.92**
Oc	6.72	**52.08**	**51.46**	**50.88**	**50.49**	**26.01**	**51.84**	**51.56**	**50.99**
Od	**10.03**	2.12	1.34	1.01	0.75	6.94	2.76	1.57	1.19
					LUMO				
X	0.00	0.00	0.00	0.00	0.00	0.00	0.00	0.00	0.00
Oa	0.01	0.01	0.00	0.01	0.01	0.01	0.02	0.01	0.00
W	**75.39**	**75.28**	**74.99**	**74.71**	**74.48**	**75.60**	**75.29**	**74.99**	**74.73**
Ob	**11.62**	**11.69**	**11.79**	**11.93**	**12.04**	**11.68**	**11.69**	**11.78**	**11.88**
Oc	**12.80**	**12.89**	**13.08**	**13.23**	**13.35**	**12.61**	**12.91**	**13.11**	**13.28**
Od	0.19	0.15	0.14	0.13	0.11	0.12	0.13	0.13	0.12

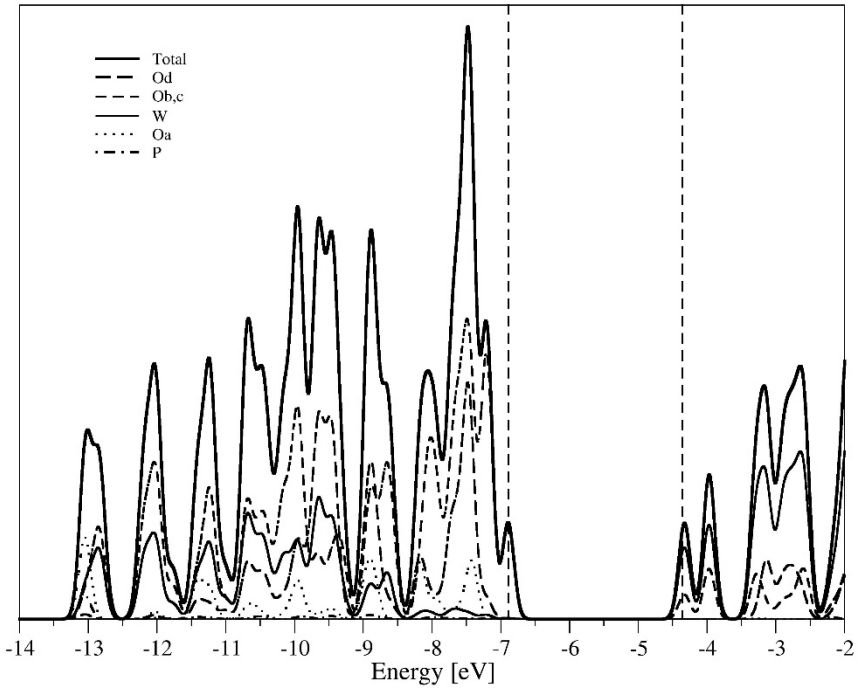

Figure 2. Total and partial density of states for $PW_{12}O_{40}^{3-}$.

Figure 3 summarizes spectra of the partial density of states (coming from Oa and central ions orbitals) for systems having the same formal oxidation state of 3+ and belonging to the same third group of the periodic table. The analysis of the spectra leads to the conclusion that Oa orbitals are included only in the valence band, whereas the conduction band consist mainly of the orbitals of central ions. The participation of Oa orbitals in valence band is similar for all three elements of B, Al, and Ga, larger near the Fermi level and decreasing with the transition to areas with lower energy. The partial atom spectra of Oa oxygen ions coordinated with B^{3+} is slightly different from the image of Al and B, which applies both to the shape and position (*2p* orbitals of Oa oxygen ions in the BW system are located the closest to the Fermi level).

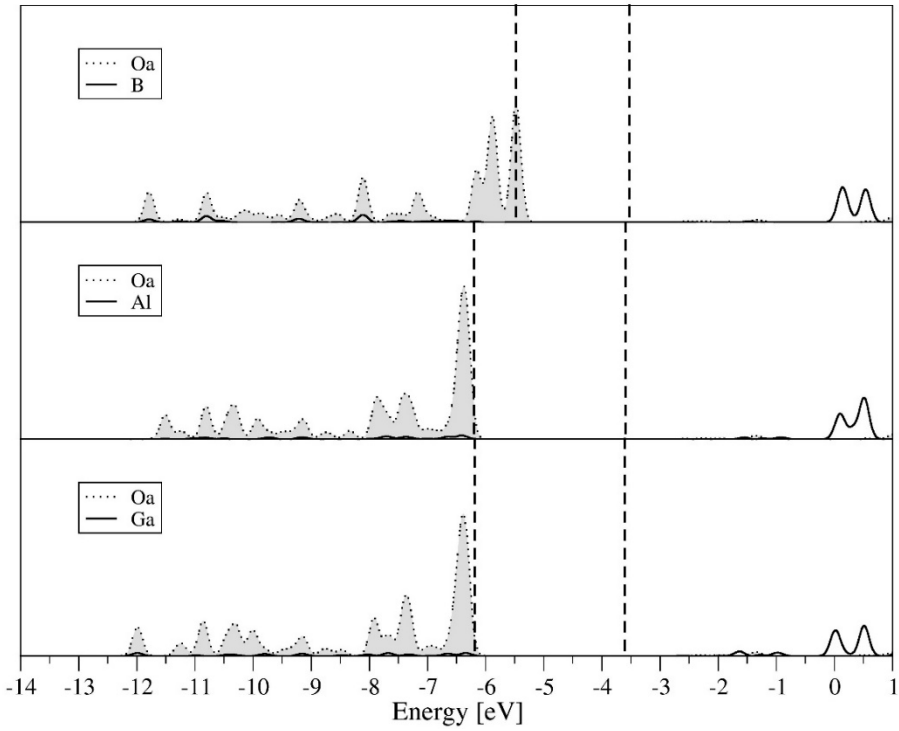

Figure 3. Partial (Oa and X atomic) density of states for $XW_{12}O_{40}{}^{3-}$, where X = B^{3+}, Al^{3+}, Ga^{3+}.

Comparison of the elements that belong to the same, third and fourth periods, respectively, which are presented in Figure 4a,b, show a strong variation in the position and the participation of orbitals coming from central ions and internal Oa oxygen ions. With the increase in electronegativity of the central ions (moving from Al to S in the third period and from Zn to As in the fourth period), the levels of frontier orbitals are shifting towards lower energies. Major changes are observed in the partial atomic spectra of oxygen ions coordinated with central ions. The partial density of states corresponding to oxygen ions coordinated with central ions decreases with increasing electronegativity of these ions (the transition from left to right of the periodic table). In the case of Al or Ga the part matching Oa oxygen ions is strongly visible in the vicinity of the Fermi level and is declining in areas with lower energy; while for the oxygen ions coordinated with S or As, it is almost identical throughout the whole area of the valence band. Partial density of states, belonging to the central ions, which appear in the conduction band increases with the increase in elements electronegativity (particularly visible for S and As). Zn is an element in which atomic spectrum is completely different from the other elements. *3d* orbitals of Zn central ion, and *2p* orbitals from the internal Oa oxygen centers, are strongly present in the valence band.

Data collected in Table 1, obtained for two solvents (acetonitrile and water), indicate that the reaction environment has a significant impact on the energy of HOMO and LUMO orbital. Extending the investigation to a wider range of solvents with dielectric constant, changing in the range from 1 to 100 (εH_2O = 80, εCH_3CN = 38.8, ε $(CH_3)_2CO$ = 20.7, εCH_3OH = 32.7, $\varepsilon(CH_3)_2SO$ = 46.7) confirms the influence of the solvent on the energy of frontier orbitals and clarifies the need of the solvent effect to be considered in theoretical calculations. Figure 5 shows the theoretically obtained energy of frontier orbitals (HOMO, LUMO) and the size of the energy band gap versus the value of the dielectric constant (ε), characterizing the selected solvent, for the reference system $PW_{12}O_{40}{}^{3-}$. From the analysis of Figure 5, one can conclude that both HOMO and LUMO energies decrease with increasing dielectric constant (ε). Changes are particularly evident in the interval of the dielectric constant (ε) from 1 to 20, whereas after exceeding ε = 20, discussed energies change insignificantly.

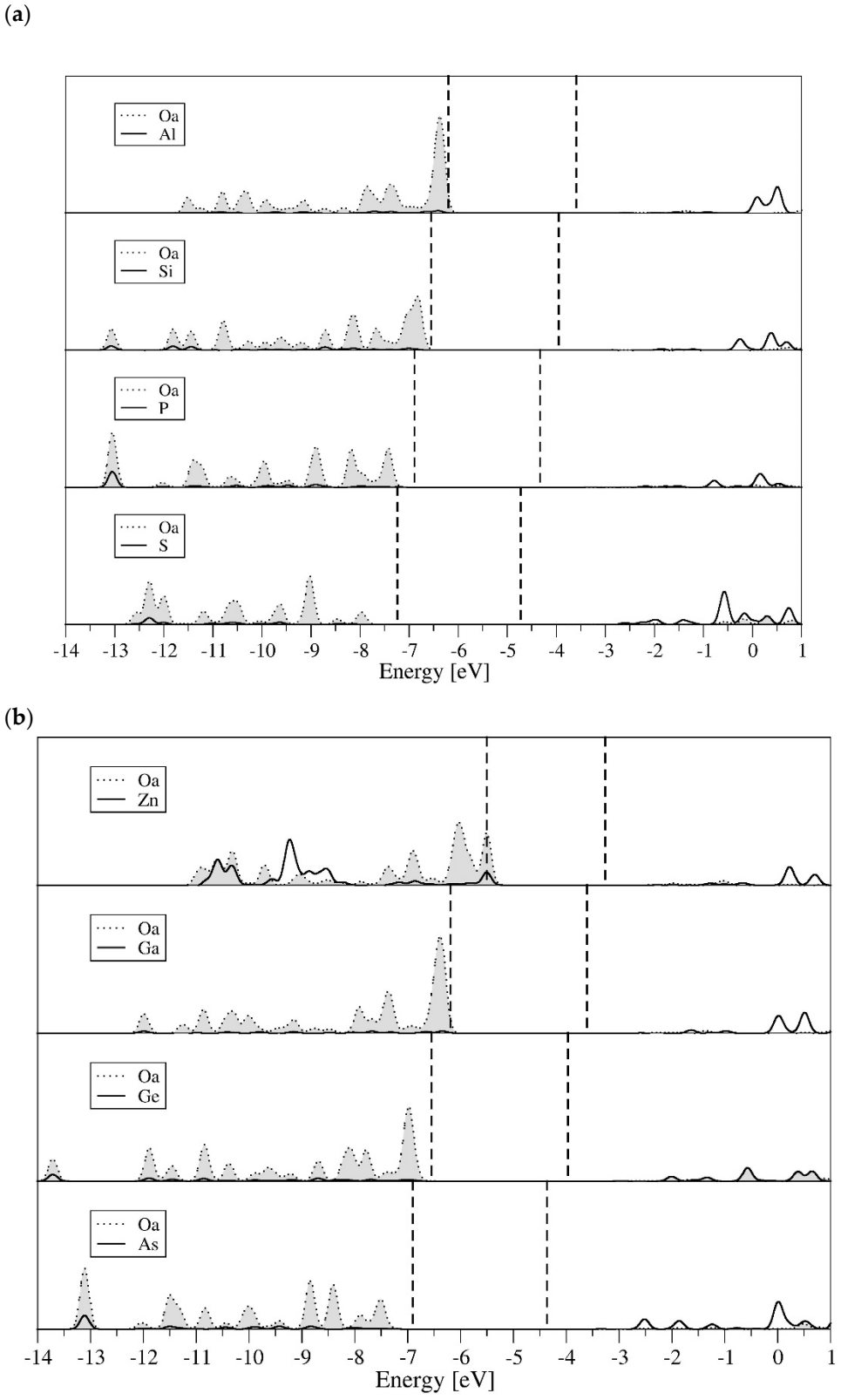

Figure 4. Partial (Oa and X atomic) density of states for systems with central ion belonging to third (**a**) and fourth (**b**) row of periodic table.

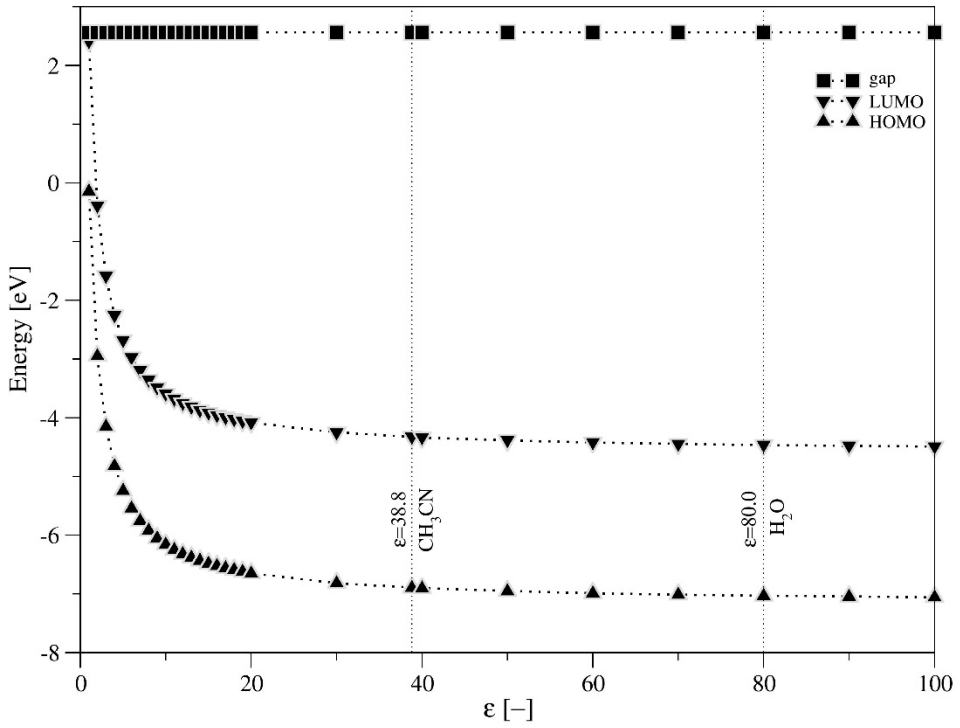

Figure 5. The relationship between values of dielectric constant and theoretically obtained energies of frontier orbitals and of band gap size for $PW_{12}O_{40}^{3-}$ as reference system. Typical solvents used for HPA acetonitrile (εCH_3CN = 38.8), water (εH_2O = 80.0), acetone ($\varepsilon(CH_3)_2CO$ = 20.7), methanol (εCH_3OH = 32.7), and DMSO ($\varepsilon(CH_3)_2SO$ = 46.7) are marked.

The detailed analysis of the orbitals in the valence band, presented above, together with the indication of the participation of orbitals of both: the central ion X and coordinated with them orbitals of Oa oxygen atoms, prompted us to determine an additional theoretical parameter that distinguish these two (X, Oa) elements. Based on the geometric structure of the Keggin anion, in which the internal tetrahedron, XO_4^n is surrounded by metal–oxygen skeleton $W_{12}O_{36}$, the interaction energy between these two building elements was determined. By applying the Energy Decomposition Analysis, the total interaction energy between the internal tetrahedron (XO_4^n) and the metal–oxygen framework ($W_{12}O_{36}$) was taken into consideration. Due to the lack of covalent bond (previous analysis of bond orders) between the internal tetrahedron (XO_4^{n-}) and metal–oxygen framework ($W_{12}O_{36}$), only the total interaction energy (ΔE_{int}) was used, without taking into account its individual contributions. The calculations were made taking into account the solvation correction with ε = 38.8 in CH_3CN, for which experimental redox potential values are available. The results are summarized in Table 1 in the penultimate row. The collected values show the dependence of the determined values of E_{int} on the substituted heteroatom X. Moving from Zn^{2+} to S^{6+}, the energy of the total interaction varies from −1.122 a.u. to −0.145, respectively. Calculated values of total energy interaction were compared with values of the redox potential obtained experimental [84]. From correlation presented in Figure 6, it is evident that the increase in ΔE_{int} energy simultaneously causes increase in redox potential; as a result, oxidizing power of heteropolyanion strengthens. Based on ΔE_{int} for two boundary systems, with the highest ($ZnW_{12}O_{40}^{6-}$) and the lowest anion charge ($SW_{12}O_{40}^{2-}$), −1.122 a.u. and −0.145 a.u., respectively, one can conclude that $SW_{12}O_{40}^{2-}$ system shows the highest oxidizing power, whereas $ZnW_{12}O_{40}^{6-}$ the weakest one. The results presented in Figure 6 that show a linear correlation (R^2 = 0.987) between both parameters, allows to define another, new theoretical parameter, which allows to quantify the redox potential of systems with a different central ion.

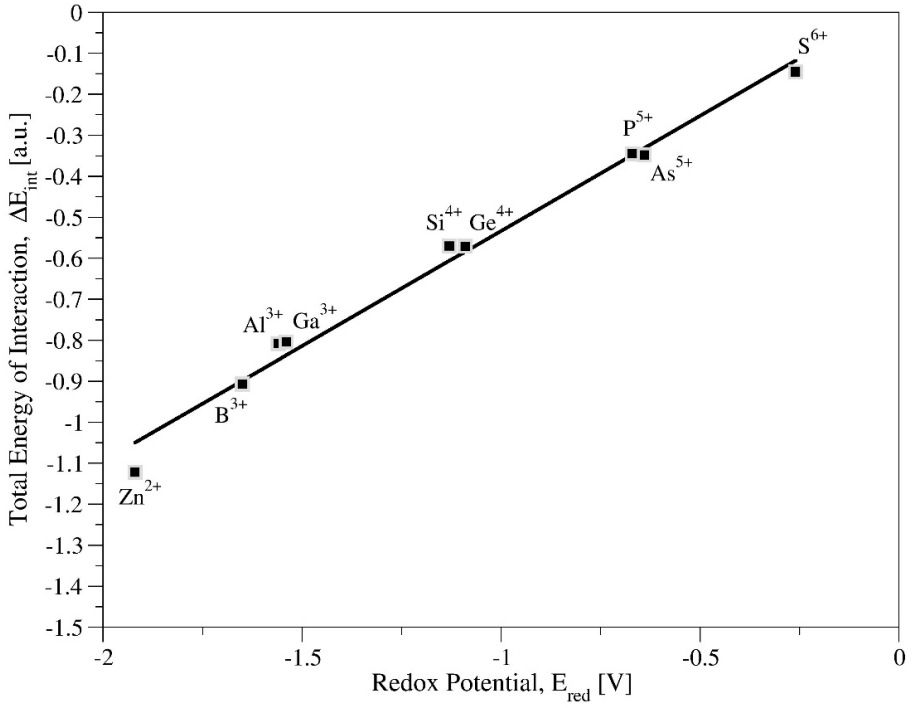

Figure 6. Correlation between total interaction energy ΔE_{int} (a.u.) and experimentally obtained [84] redox potential E_{red} (V), for $XW_{12}O_{40}^{n-}$ in CH_3CN as a solution.

2.2. $XMo_{12}O_{40}^{n-}$ Systems

Similar type of calculations was carried out for molybdenum heteropolyanions $XMo_{12}O_{40}^{n-}$ modified in position of heteroatom by various elements X = Zn^{2+}, B^{3+}, Al^{3+}, Ga^{3+}, Si^{4+}, Ge^{4+}, P^{5+}, As^{5+}, and S^{6+}. Tables 3 and 4 present energies of frontier (HOMO, LUMO) orbitals, E_{HOMO} and E_{LUMO} (eV), the band gap for $XMo_{12}O_{40}^{n-}$ systems in vacuum and in solvents (water and acetonitrile) as well as atomic composition of frontier orbitals, for all studied systems.

Table 3. Energies of frontier (HOMO, LUMO) orbitals, E_{HOMO} and E_{LUMO} (eV) and the band gap for $XMo_{12}O_{40}^{n-}$ systems in vacuum, water, and acetonitrile-CH_3CN (top, middle, and bottom part of the table, respectively). Additionally total energy, ΔE_{int} (a.u.), for $XMo_{12}O_{40}^{n-}$ system in acetonitrile, are presented (in last row).

X	Zn^{2+}	B^{3+}	Al^{3+}	Ga^{3+}	Si^{4+}	Ge^{4+}	P^{5+}	As^{5+}	S^{6+}
					Vacuum				
E_{HOMO}	8.20	6.18	5.47	5.45	2.81	2.78	0.10	0.07	−2.65
E_{LUMO}	10.73	8.00	7.96	7.95	5.14	5.13	2.30	2.29	−0.55
Gap	2.53	1.82	2.49	2.50	2.33	2.35	2.20	2.22	2.10
					Water (H_2O)				
E_{HOMO}	−5.87	−5.61	−6.32	−6.33	−6.59	−6.61	−6.90	−6.88	−7.19
E_{LUMO}	−3.38	−3.84	−3.82	−3.81	−4.25	−4.24	−4.68	−4.67	−5.08
Gap	2.49	1.77	2.50	2.52	2.34	2.37	2.22	2.21	2.11
					Acetonitrile (CH_3CN)				
E_{HOMO}	−5.87	−5.37	−6.08	−6.09	−6.40	−6.42	−6.74	−6.76	−7.10
E_{LUMO}	−3.38	−3.60	−3.58	−3.57	−4.06	−4.05	−4.54	−4.53	−4.99
Gap	2.48	1.77	2.50	2.52	2.34	2.37	2.20	2.23	2.10
ΔE_{int} (a.u.)	−1.248	−0.900	−0.796	−0.795	−0.660	−0.643	−0.443	−0.448	−0.254

ΔE_{int}—total energy interaction between the internal tetrahedron (XO_4^{n-}) and the metal–oxygen framework ($Mo_{12}O_{36}$).

Table 4. Decomposition into atomic contribution (in %) of HOMO and LUMO orbitals in $XMo_{12}O_{40}^{n-}$ system.

X	B^{3+}	Al^{3+}	Si^{4+}	P^{5+}	S^{6+}	Zn^{2+}	Ga^{3+}	Ge^{4+}	As^{5+}
					HOMO				
X	0.00	0.00	0.00	0.00	0.00	10.82	0.00	0.00	0.00
Oa	**76.12**	0.12	0.02	0.01	0.01	**49.90**	0.23	0.11	0.01
W	5.79	1.65	1.70	1.89	2.19	2.01	1.70	1.74	1.96
Ob	1.89	**41.47**	**43.51**	**44.86**	**45.80**	2.52	**40.82**	**45.47**	**44.25**
Oc	5.82	**55.13**	**53.54**	**52.27**	**51.24**	**24.20**	**55.46**	**51.21**	**52.72**
Od	**10.39**	1.63	1.23	0.98	0.76	10.56	1.78	1.47	1.05
					LUMO				
X	0.00	0.00	0.00	0.00	0.00	0.00	0.00	0.00	0.00
Oa	0.06	0.03	0.02	0.01	0.00	0.02	0.02	0.00	0.00
W	**70.29**	**69.74**	**70.10**	**70.34**	70.44	**69.33**	**69.62**	**71.83**	**70.16**
Ob	**14.45**	**15.04**	**14.64**	**14.34**	**14.13**	**15.46**	**15.11**	**12.92**	**14.51**
Oc	**14.14**	**14.14**	**14.44**	**14.73**	**14.99**	**13.99**	**14.19**	**15.01**	**14.72**
Od	1.05	1.05	1.23	0.58	0.44	1.20	1.06	0.27	0.61

The calculated parameters differ quantitatively from those obtained for XW; nevertheless, the changes observed during transitions between groups or within groups are qualitatively identical for both XW and XMo systems. This suggests that the methodology used for XW systems (linear correlation between E_{LUMO}/E_{int} and redox potential) can also be apply to the XMo system.

Based on the relationship between E_{LUMO} and charge of the central ion, found for the XW and XMo systems, the dependence of XW vs. XMo was determined. Next, using the correlation between E_{LUMO} vs. redox potential obtained for XW systems in acetonitrile and on the previously figured mathematical relationship between XW and XMo, the predicted redox potential values for XMo systems were found (details are described in the Supplementary Materials). The values are collected in Table 5, where additionally the last line presents the experimentally determined redox potential values taken from the literature [85].

Table 5. Redox potential appointed using theoretical methods and experimentally obtained [85] redox potentials for molybdenum $XMo_{12}O_{40}^{n-}$ heteropolyanions in acetonitrile (CH_3CN).

X.	Al^{3+}	Ga^{3+}	Si^{4+}	Ge^{4+}	P^{5+}	As^{5+}	S^{6+}
				CH_3CN			
Model	−1.56	−1.54	−1.10	−1.08	−0.63	−0.64	−0.21
E_{red} (eV)	-	-	−1.10	−1.14	−0.64	−0.66	−0.11

The comparison of the values obtained from the mathematical model and those taken from the experimental measurements clearly shows that the mathematical model works properly, and the predicted redox potential values for most of the central ions are almost identical to the experimental data (the only exception is S, for which the predicted redox potential value is almost twice as high as the measured value).

This allows us to assume that the mutual similarities and the correlations between the theoretical parameters calculated for the XW and XMo systems form the basis for the qualitative and quantitative prediction of redox potential being one of the possible parameters describing catalytic properties.

3. Materials and Methods

One can find many HPA systems with different structures but the most important for catalysis are those containing one central atom/heteroatom and twelve metal/addenda ions; known as Keggin anions described by the general formula $Y_nXM_{12}O_{40}$. In this partic-

ular structure, the central position is occupied by ion, X, coordinated to four oxygen atoms, forming internal tetrahedron XO_4^{n-}. Tetrahedron is surrounded by twelve edge- and corner-sharing metal–oxygen octahedral MO_6, which are arranged in four M_3O_{13} groups, each formed by three octahedral sharing edges and having common oxygen atom, which is also shared with central XO_4 tetrahedron (Figure 7).

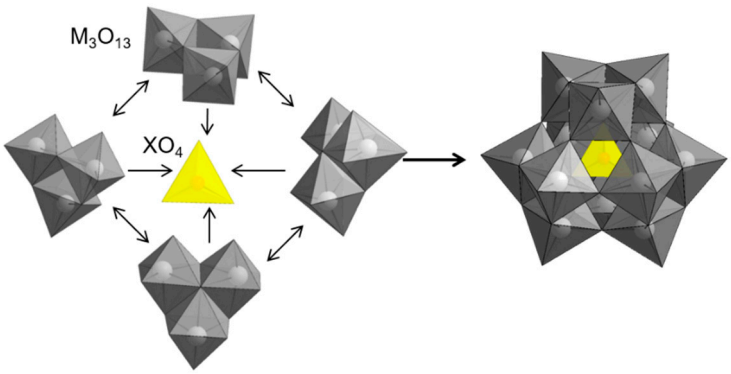

Figure 7. Geometries of building elements of Keggin anion.

To model the influence of central ion substitution on the oxidizing power of modified molybdenum and tungsten heteropolyacids, a series of p-block elements were selected; in addition, zinc was also taken into consideration. The main selection criterion was the availability of experimental values of redox potentials obtained for a series of compounds in the same conditions to eliminate other parameters. Electronic structure calculations were performed for $XW_{12}O_{40}^{n-}$ and $XMo_{12}O_{40}^{n-}$ Keggin anions modified in position of heteroatom, by various elements X = Zn^{2+}, B^{3+}, Al^{3+}, Ga^{3+}, Si^{4+}, Ge^{4+}, P^{5+}, As^{5+}, and S^{6+}. The examined central ions can be ordered according to several criteria. One of them is to divide central ions according to which row of periodic table they belong to. In such a case, the studied systems can be divided into three groups. In the first group the central ion B^{3+} belongs to II row, in the second group central ion belongs to III row (Al^{3+}, Si^{4+}, P^{5+}, and S^{6+}) and in the third group the central ion lies in IV row (Zn^{2+}, Ga^{3+}, Ge^{4+}, and As^{5+}). The other possibility is to group central ions according to their formal oxidation state that is equal to formal charge of internal tetrahedron (XO_4^{n-}) and, thus, the global charge of Keggin anion. As a result, one obtains five groups where n = 2 (S^{6+}), n = 3 (P^{5+} As^{5+}), n = 4 (Si^{4+}, Ge^{4+}), n = 5 (B^{3+}, Al^{3+}, and Ga^{3+}), and n = 6 (Zn^{2+}). However, in our opinion the most proper and adequate solution to the problem is not to divide elements into any group but to take into consideration their position in the periodic table.

The calculations were based on DFT theory and local cluster model. Exchange and correlation energies were calculated using the Perdew–Burke–Ernzenhof functional within the generalized gradient corrected approximation (GGA-PBE) [86] (Turbomole code [87]). The TZVP (basis sets of triple-zeta valence with polarization) base was applied for all elements except transition metal ions (W, Mo) where pseudopotentials were used [88].

Geometry optimizations were performed according to quasi-Newton–Raphsod method within BFGS algorithm proposed by Broyden [89], Fletcher [90], Goldfarb [91], and Shanno [92] independently. Obtained converged geometry satisfies the following parameters: (a) the energy change between two optimization cycles drops below 10^{-6} a.u., (b) the maximum displacement element drops below 10^{-3} a.u., and (c) the maximum gradient element dropped below 10^{-3} a.u.

Different spin states for all systems were checked by performing spin restricted and unrestricted calculations for the close and open shell anions, respectively. In the discussion below only the systems with lowest total energy are discussed, all being singlet states.

The solvation effect was included by COSMO approximation [93] (COnductorlike Screening MOdel) where the solute molecule forms a cavity within the dielectric continuum of permittivity ε (for ideal solvent $\varepsilon = \infty$) that represents the solvent. The cavity construction starts with a union of spheres of radii $R_i + R_{solv}$ for all atoms i.

Interaction between internal tetrahedron (XO_4^{n-}) and metal–oxygen framework was performed according to energy decomposition analysis scheme (EDA) developed by Morokuma [94] and by Ziegler and Rauk [95].

4. Conclusions

The presented results of calculations show that the type of central ion influences both the energy levels of boundary orbitals and the size of band gap, parameters which determine the oxidation-reduction potential of heteropolyacids systems. The comparison of theoretical and experimental data leads to the conclusion that theoretical energy of LUMO orbitals (obtained for systems in solvent) gives an important information about the redox potential of the system.

Moreover, a total energy interaction (ΔE_{int}) can be a proper theoretical parameter to reflect the oxidizing ability of heteropolyanions modified in the central ion position in both tungsten and molybdenum systems.

The analysis of density of states spectra clearly shows that the effect of the central ion on the energy of frontier orbitals of heteropolyacids anions takes place through the various oxygen centers present in the area of the valence energy near the Fermi level, the characteristics of which change along with the type of the central ion. The participation of both the central ion orbitals and the Oa oxygen orbitals directly coordinated with it, in the zone close to the valence level, unequivocally explains the influence of the X ion on the energy of the boundary orbitals and the size of the energy gap.

Supplementary Materials: The following supporting information can be downloaded. Figure S1: Correlation between en-ergy of LUMO (Lowest Unoccupied Molecular Orbitals) orbitals, ELUMO (eV), and charge of central ions, X, for $XW_{12}O_{40}^{n-}$ (XW—blue squares) and $XMo_{12}O_{40}^{n-}$ (XMo—red squares) systems n = 2–5, in CH3CN as a solution, where the central ions, X = Al^{3+}, Si^{4+}, P^{5+}, S6+; Figure S2: Corre-lation between energy of LUMO (Lowest Unoccupied Molecular Orbitals) orbitals, ELUMO (eV), and experimental [85] redox potential [V] for $XW_{12}O_{40}^{n-}$ (XW) systems n = 2–5, in CH3CN as a solution, where the central ions, where X = Al^{3+}, Si^{4+}, P^{5+}, S^{6+}; Table S1: Energy of LUMO (Lowest Occupied Molecular Orbital) orbitals, ELUMO, [eV] for XW12O40^{n-} (XW) and $XMo_{12}O_{40}^{n-}$ (XMo) systems n = 2–5, in CH3CN as a solution, where X = Al^{3+}, Si^{4+}, P^{5+}, S^{6+} (the central ion belongs to the III period of the periodic table); Table S2: Successive coordinates for $XMo_{12}O_{40}^{n-}$ (XMo) systems n = 2–5, in CH3CN as a solution, where the central ions, X = Al^{3+}, Si^{4+}, P^{5+}, S^{6+}, determined in the mathematical model, from the dependence of straight lines ob-tained for the XW and XMo systems from Figure S1.

Author Contributions: Conceptualization, methodology, validation, formal analysis, investigation, and writing—original draft preparation R.T.-S. and P.N.; software, visualization, resources, and data curation, P.N.; supervision and project administration R.T.-S.; writing—review and editing, and funding acquisition R.T.-S., P.N. and M.W. All authors have read and agreed to the published version of the manuscript.

Funding: P.N. partially financed by funds University of Applied Sciences in Tarnow, PWSZ/PRNRs/0700-5/PN-U/2021; The work of R.T.-S. and M.W. was done within the statutory funds of the Jerzy Haber Institute of Catalysis and Surface Chemistry Polish Academy of Sciences. This research was supported in part by PLGrid Infrastructure.

Institutional Review Board Statement: Not applicable.

Informed Consent Statement: Not applicable.

Data Availability Statement: Data are provided by the authors upon a reasonably request.

Conflicts of Interest: The authors declare no conflict of interest.

Sample Availability: Not applicable.

References

1. Kozhevnikov, I.V. Catalysis by Heteropoly Acids and Multicomponent Polyoxometalates in Liquid-Phase Reactions. *Chem. Rev.* **1998**, *98*, 171–198. [CrossRef] [PubMed]
2. Kozhevnikov, I.V. Sustainable heterogeneous acid catalysis by heteropoly acids. *J. Mol. Catal. A Chem.* **2007**, *262*, 86–92. [CrossRef]
3. Kozhevnikov, I.V. Heterogeneous acid catalysis by heteropoly acids: Approaches to catalyst deactivation. *J. Mol. Catal. A Chem.* **2009**, *305*, 104–111. [CrossRef]
4. Timofeeva, M.N.; Matrosova, M.M.; Maksimov, G.M.; Likholobov, V.A. A Study of the Acid Properties of Structurally and Compositionally Different Heteropoly Acids in Acetic Acid. *Kinet. Catal.* **2001**, *42*, 785–790. [CrossRef]
5. Timofeeva, M.N. Acid Catalysis by Heteropoly Acids. *Appl. Catal. A Gen.* **2003**, *256*, 19–35. [CrossRef]
6. Tanaka, K.-I.; Ozaki, A. Acid-Base Properties and Catalytic Activity of Solid Surfaces. *J. Catal.* **1967**, *8*, 1–7. [CrossRef]
7. Rhule, J.T.; Hill, C.L.; Judd, D.A. Polyoxometalates in Medicine. *Chem. Rev.* **1998**, *98*, 327–357. [CrossRef]
8. Muller, F.; Peters, F.; Pope, M.T.; Gatteschi, D. Polyoxometalates: Very Large Clusters-Nanoscale Magnets. *Chem. Rev.* **1998**, *98*, 239–271. [CrossRef]
9. Mizuno, N.; Misono, M. Heterogeneous Catalysis. *Chem. Rev.* **1998**, *98*, 199–217. [CrossRef]
10. Misono, M.; Ono, I.; Koyano, G.; Aoshima, A. Heteropolyacids. Versatile green catalysts usable in a variety of reaction media. *Pure Appl. Chem.* **2000**, *72*, 1305–1311. [CrossRef]
11. Misono, M. Acid catalysts for clean production. Green aspects of heteropolyacid catalysts. *C. R. L'académie Sci. Ser. IIC-Chem.* **2000**, *3*, 471–475. [CrossRef]
12. Klemperer, W.G.; Wall, C.G. Polyoxoanion Chemistry Moves toward the Future: From Solids and Solutions to Surfaces. *Chem. Rev.* **1998**, *98*, 297–306. [CrossRef]
13. Izumia, Y.; Urabe, K.; Onaka, M. Recent advances in liquid-phase organic reactions using heteropolyacid and clay. *Catal. Surv. Jpn.* **1997**, *1*, 17–23. [CrossRef]
14. Heravi, M.M.; Sadjadi, S. Recent Developments in Use of Heteropolyacids, Their Salts and Polyoxometalates in Organic Synthesis. *J. Iran. Chem. Soc.* **2009**, *6*, 1–54. [CrossRef]
15. Coronado, E.; Gomez-Garcia, C.J. Polyoxometalate-Based Molecular Materials. *Chem. Rev.* **1998**, *98*, 273–296. [CrossRef]
16. Melsheimer, J.; Mahmoud, S.S.; Mestl, G.; Schlogl, R. In Situ UV-VIS diffuse reflectance spectroscopy of reduction–reoxidation of heteropoly compounds by methanol and ethanol: A correlation between spectroscopic and catalytic data. *Catal. Lett.* **1999**, *60*, 103–111. [CrossRef]
17. Kaba, M.S.; Song, I.K.; Barteau, M.A. Ordered Array Formation and Negative Differential Resistance Behavior of Cation-Exchanged Heteropoly Acids Probed by Scanning Tunneling Microscopy. *J. Phys. Chem.* **1996**, *100*, 19577–19581. [CrossRef]
18. Kaba, M.S.; Song, I.K.; Barteau, M.A. Investigation of Framework and Cation Substitutions in Keggin-type Heteropoly Acids Probed by Scanning Tunneling Microscopy and Tunneling Spectroscopy. *J. Vac. Sci. Technol. A* **1997**, *15*, 1299–1304. [CrossRef]
19. Song, I.K.; Kaba, M.S.; Barteau, M.A.; Lee, W.Y. Investigation of Redox Potential and Negative Differential Resistance Behavior of Heteropolyacids by Scanning Tunneling Microscopy. *Catal. Today* **1998**, *44*, 285–291. [CrossRef]
20. Kinne, M.; Barteau, M.A. STM and TS investigations of silver polyoxometalate monolayers: Model compounds and potential. *Surf. Sci.* **2000**, *447*, 105–111. [CrossRef]
21. Song, I.K.; Barteau, M.A. Bulk redox properties of heteropolyacids determined from surface properties of nanostructured heteropolyacid monolayers. *J. Mol. Catal. A Chem.* **2002**, *182–183*, 185–193. [CrossRef]
22. Song, I.K.; Shnitser, R.B.; Cowan, J.J.; Hill, C.L.; Barteau, M.A. Nanoscale Characterization of Redox and Acid Properties of Keggin-Type Heteropolyacids by Scanning Tunneling Microscopy and Tunneling Spectroscopy: Effect of Heteroatom Substitution. *Inorg. Chem.* **2002**, *41*, 1292–1298. [CrossRef]
23. Okuhara, T.; Mizuno, N.; Misono, M. Catalytic Chemistry of Heteropoly Compounds. *Adv. Catal.* **1996**, *41*, 113–252.
24. Grigoriev, V.A.; Hill, C.L.; Weinstock, I.A. Role of Cation Size in the Energy of Electron Transfer to 1:1 Polyoxometalate Ion Pairs $\{(M^+)(X^{n+}VW_{11}O_{40})\}^{(8-n)-}$ (M = Li, Na, K). *J. Am. Chem. Soc.* **2000**, *122*, 3544–3545. [CrossRef]
25. Sadakane, M.; Steckhan, E. Electrochemical Properties of Polyoxometalates as Electrocatalysts. *Chem. Rev.* **1998**, *98*, 219–237. [CrossRef] [PubMed]
26. Eguchi, K.; Seiyama, T.; Yamazoe, N.; Katsuki, S.; Taketa, H. Electronic Structures of $XMo_{12}O_{40}$ Heteropolyanions (X = P, As, Si, and Ge) and Their Reduction Behavior. *J. Catal.* **1988**, *111*, 336–344. [CrossRef]
27. Pope, M.T.; Varga, G.M., Jr. Heteropoly Blues. I. Reduction Stoichiometries and Reduction Potentials of Some 12-Tungstates. *Inorg. Chem.* **1966**, *5*, 1249–1254.
28. Altenau, J.J.; Pope, M.T.; Prados, R.A.; So, H. Models for Heteropoly Blues. Degrees of Valence Trapping in Vanadium (lV)—And Molybdenum(V)—Substituted Keggin Anions. *Inorg. Chem.* **1975**, *14*, 417–421. [CrossRef]
29. Song, I.K.; Barteau, M.A. Redox properties of kegging-type heteropolyacid (HPA) catalysts: Effect of counter-cation, heteroatom, and polyatom substitution. *J. Mol. Catal. A Chem.* **2004**, *212*, 229–236. [CrossRef]
30. Lee, L.; Wang, J.X.; Adzic, R.R.; Robinson, I.K.; Gewirth, A.A. Adsorption configuration and local ordering of silicotungstate anions on Ag(100) electrode surfaces. *J. Am. Chem. Soc.* **2001**, *123*, 8838–8843. [CrossRef]
31. Himeno, S.; Osakai, T.; Saito, A. Voltammetric characterization of alpha and beta-dodecamolybdophosphates in aqueous organic solutions. *Bull. Chem. Soc. Jpn.* **1989**, *62*, 1335–1337. [CrossRef]

32. Kaba, M.S.; Song, I.K.; Wasfi, S.H.; Barteau, M.A. Investigation of Wells-Dawson Heteropoly Oxofluorotungstates by Scanning Tunneling Microscopy and Tunneling Spectroscopy. *J. Electrochem. Soc.* **2002**, *149*, E117. [CrossRef]
33. Lopez, X.; Poblet, J.M. DFT Study on the Five Isomers of $PW_{12}O_{40}^{3-}$: Relative Stabilization upon Reduction. *Inorg. Chem.* **2004**, *43*, 6863–6865. [CrossRef]
34. Lopez, X.; Fernandez, J.A.; Poblet, J.M. Redox properties of polyoxometalates: New insights on the anion charge effect. *Dalton Trans.* **2006**, *9*, 1162–1167. [CrossRef]
35. Lopez, X.; Fernandez, J.A.; Romo, S.; Paul, J.F.; Kazansky, L.; Poblet, J.M. Are the solvent effects critical in the modeling of polyoxoanions? *J. Comput. Chem.* **2004**, *25*, 1542–1549. [CrossRef]
36. Pope, M.T. *Heteropoly and Isopoly Oxometalates*; Springer: New York, NY, USA, 1983.
37. Mbomekalle, I.-M.; Lopez, X.; Poblet, J.M. Influence of the Heteroatom Size on the Redox Potentials of Selected Polyoxoanions. *Inorg. Chem.* **2010**, *49*, 7001–7006. [CrossRef] [PubMed]
38. Song, Y.-F.; Tsunashima, R. Recent advances on polyoxometalate-based molecular and composite materials. *Chem. Soc. Rev.* **2012**, *41*, 7384–7402. [CrossRef] [PubMed]
39. Dolbecq, A.; Dumas, E.; Mayer, C.R.; Mialane, P. Hybrid organic-inorganic polyoxometalate compounds: From structural diversity to applications. *Chem. Rev.* **2010**, *110*, 6009–6048. [CrossRef] [PubMed]
40. Batten, S.R.; Champness, N.R.; Chen, X.-M.; Garcia-Martinez, J.; Kitagawa, S.; Öhrström, L.; O'Keeffe, M.; Paik Suh, M.; Reedijk, J. Terminology of metal-organic frameworks and coordination polymers (IUPAC Recommendations 2013). *Pure Appl. Chem.* **2013**, *85*, 1715–1724. [CrossRef]
41. He, W.-W.; Li, S.-L.; Zang, H.-Y.; Yang, G.-S.; Zhang, S.-R.; Su, Z.-M.; Lan, Y.-Q. Entangled structures in polyoxometalate-based coordination polymers. *Coord. Chem. Rev.* **2014**, *279*, 141–160. [CrossRef]
42. Wang, X.; Tian, A.; Wang, X. Architectural chemistry of polyoxometalate-based coordination frameworks constructed from flexible N-donor ligands. *RSC Adv.* **2005**, *5*, 41155–41168. [CrossRef]
43. Gong, P.; Li, Y.; Luo, J.; Chen, L.; Zhao, J. Syntheses, structures and properties of two copper-2-picolinic-acid germanomolybdate hybrids with mixed organic components. *Inorg. Chem. Commun.* **2016**, *71*, 113–118. [CrossRef]
44. Li, L.; Cheng, M.; Bai, Y.; An, B.; Dang, D. A polyoxometalate-based inorganic–organic hybrid polymer constructed from silver-Schiff base building block and Keggin-type cluster: Synthesis, crystal structure and photocatalytic performance for the degradation of rhodamine B. *Spectrochim. Acta Part A Mol. Biomol. Spect.* **2015**, *150*, 846–854. [CrossRef]
45. Tian, A.; Ning, Y.; Ying, J.; Zhang, J.; Hou, X.; Li, T.; Wang, X. Highly efficient usage of the hydrothermal technique through the one-pot method to construct four Keggin-based compounds containing pendent ligands. *Dalton Trans.* **2015**, *44*, 10499–10507. [CrossRef] [PubMed]
46. Wang, X.; Li, T.; Tian, A.; Xu, N.; Zhang, R. Introduction of secondary pyridyl-1H-tetrazole derivatives into Keggin–Ag–(1,10-phenanthroline) system for tuning dimensionalities and architectures: Assembly and properties. *J. Coord. Chem.* **2016**, *69*, 2532–2544. [CrossRef]
47. Zhao, C.; Li, S.; Ma, H.; Zhang, C.; Pang, H.; Yu, Y.; Zhang, Z. The factors affecting the assembly of Keggin–metal–bimb systems: Charge/polarity of Keggin polyanions and coordination modes of metal cations. *CrystEngComm* **2016**, *18*, 6233–6244. [CrossRef]
48. Li, L.; Sun, J.-W.; Sha, J.-Q.; Li, G.-M.; Yan, P.-F.; Wang, C.; Yu, L. Structure refinement and photocatalytic properties of porous POMCPs by selecting the isomerous PYTTZ. *Dalton Trans.* **2015**, *44*, 1948–1954. [CrossRef] [PubMed]
49. Hao, H.-F.; Zhou, W.-Z.; Zang, H.-Y.; Tan, H.-Q.; Qi, Y.-F.; Wang, Y.-H.; Li, Y.-G. Keggin-Type Polyoxometalate-Based Metal–Organic Networks for Photocatalytic Dye Degradation. *Chem. Asian J.* **2015**, *10*, 1676–1683. [CrossRef] [PubMed]
50. Zhao, X.; Zhang, S.; Yan, J.; Li, L.; Wu, G.; Shi, W.; Yang, G.; Guan, N.; Cheng, P. Polyoxometalate-based metal–organic frameworks as visible-light-induced photocatalysts. *Inorg. Chem.* **2018**, *57*, 5030–5037. [CrossRef]
51. Tian, A.-X.; Hou, X.; Ying, J.; Liu, G.-C.; Yang, Y.; Ning, Y.-L.; Li, T.-J.; Wang, X.-L. A series of polyoxometalate-based compounds including infinite Ag belts and circles constructed by two tolyl-1H-tetrazole isomers. *RSC Adv.* **2015**, *5*, 53757–53765. [CrossRef]
52. Zhou, E.-L.; Qin, C.; Wang, X.-L.; Shao, K.-Z.; Su, Z.-M. Assembly of two novel 3D organic–inorganic hybrids based on Keggin-type polyoxometalates: Syntheses, crystal structures and properties. *CrystEngComm* **2016**, *18*, 6370–6377. [CrossRef]
53. Li, M.-T.; Sha, J.-Q.; Zong, X.-M.; Sun, J.-W.; Yan, P.-F.; Li, L.; Yang, X.-N. Assembly of Polyoxometalate-Based Hybrids with Different Helical Channels upon Subtle Ligand Variation. *Cryst. Growth Des.* **2014**, *14*, 2794–2802. [CrossRef]
54. Zhao, C.; Ma, H.; Pang, H.; Li, S.; Zhang, Z.; Yu, Y. A new POMOF consisting of $[VW_{12}]^{4-}$ clusters and metal-organic nanotubes: Synthesis, structure, electrocatalytic and luminescent properties. *Inorg. Chem. Commun.* **2016**, *69*, 57–61. [CrossRef]
55. Sha, J.-Q.; Sun, L.-J.; Zhu, P.-P.; Jiang, J. The first two-fold interpenetrating polyoxometalate-based coordination polymer with helical channels: Structure and catalytic activities. *CrystEngComm* **2016**, *18*, 283–289. [CrossRef]
56. Khenkin, A.M.; Efremenko, I.; Weiner, L.; Martin, J.M.L.; Neumann, R. Photochemical Reduction of Carbon Diooxide Catalyzed by a Ruthenium-Substituted Polyoxometalate. *Chem. Eur. J.* **2010**, *16*, 1356–1364. [CrossRef] [PubMed]
57. Wang, X.-L.; Song, G.; Lin, H.-Y.; Wang, X.; Liu, G.-C.; Rong, X. Polyoxometalate-induced different metal–organic frameworks based on isonicotinic acid and Ag^{I} ion: Syntheses, structures and properties. *Inorg. Chem. Commun.* **2017**, *84*, 168–173. [CrossRef]
58. Chai, D.-F.; Wang, M.; Zhang, C.; Ning, F.; Xu, W.; Pang, H.; Ma, H. A novel 3D POMOF based on dinuclear copper (II)-oxalate complexes and Keggin polyoxoanions with excellent photocatalytic activity. *Inorg. Chem. Commun.* **2017**, *83*, 16–19. [CrossRef]
59. Sha, J.; Yang, X.; Zhu, P.; Lan, Y.; Sheng, N. Two new silver triazole frameworks with polyoxometalate templates. *RSC Adv.* **2016**, *6*, 108328–108334. [CrossRef]

60. Li, Y.-W.; Guo, L.-Y.; Su, H.-F.; Jagodic, M.; Luo, M.; Zhou, X.-Q.; Zeng, S.-Y.; Tung, C.-H.; Sun, D.; Zheng, L.-S. Two Unprecedented POM-Based Inorganic–Organic Hybrids with Concomitant Heteropolytungstate and Molybdate. *Inorg. Chem.* **2017**, *56*, 2481–2489. [CrossRef] [PubMed]
61. Luo, Y.-H.; Lu, X.-X.; Zhang, H. An ultrastable, flexible POM-based coordination polymer with redox properties. *CrystEngComm* **2014**, *16*, 7865–7868. [CrossRef]
62. Zhou, W.; Peng, J.; Zhang, Z.; Shi, Z.; Khan, S.U.; Liu, H. Assembly of hybrids based on polyoxotungstates and Co-tris(imidazolyl) complexes with bifunctional electrocatalytic activities. *RSC Adv.* **2015**, *5*, 35753–35759. [CrossRef]
63. Wang, X.-I.; Hu, H.-I.; Tian, A.-X. Influence of Transition Metal Coordination Nature on the Assembly of Multinuclear Subunits in Polyoxometalates-Based Compounds. *Cryst. Growth Des.* **2010**, *10*, 4786–4794. [CrossRef]
64. Wang, X.-L.; Gao, Q.; Tian, A.-X.; Hu, H.-L.; Liu, G.-C. Assembly of a series of Keggin-based multi- and mono-nuclear structures by tuning the bis(tetrazole)-functionalized thioether ligands. *Inorg. Chim. Acta* **2012**, *384*, 62–68. [CrossRef]
65. Zhang, Z.; Pang, H.; Ma, H.; Li, S.; Zhao, C. pH-Directed assembly of four polyoxometalate-based supramolecular hybrids by using tritopic bridging ligand 1, 3, 5-tris-(1-imidazolyl)-benzene: Structures and electrocatalytic properties. *Solid State Sci.* **2018**, *75*, 1–8. [CrossRef]
66. Tian, A.; Tian, Y.; Ning, Y.; Hou, X.; Ni, H.; Ji, X.; Liu, G.; Ying, J. A series of Keggin-based compounds constructed by conjugate ring-rich pyrazine and quinoxaline derivatives. *Dalton Trans.* **2016**, *45*, 13925–13936. [CrossRef]
67. Cao, Y.; Lv, J.; Yu, K.; Wang, C.; Su, Z.; Wang, L.; Zhou, B. Synthesis and photo-/electro-catalytic properties of Keggin polyoxometalate inorganic–organic hybrid layers based on d^{10} metal and rigid benzo-diazole/-triazole ligands. *New J. Chem.* **2017**, *41*, 12459–12469. [CrossRef]
68. Wang, C.-J.; Wang, T.-T.; Lan, Q.; Yao, S.; Wu, H.-L.; Zhou, Y.-Y.; Zhang, Z.-M.; Wang, E.-B. Polyoxometalate-based supramolecular architecture constructed from a purely inorganic 1D chain and a metal–organic layer with efficient catalytic activity. *RSC Adv.* **2016**, *6*, 15513–15517. [CrossRef]
69. Jiao, Y.-Q.; Qin, C.; Zang, H.-Y.; Chen, W.-C.; Wang, C.-G.; Zheng, T.-T.; Shao, K.-Z.; Su, Z.-M. Assembly of organic–inorganic hybrid materials constructed from polyoxometalate and metal–1,2,4-triazole units: Synthesis, structures, magnetic, electrochemical and photocatalytic properties. *CrystEngComm* **2015**, *17*, 2176–2189. [CrossRef]
70. Wang, W.; Xu, L.; Gao, G.; Liu, L.; Liu, X. The first ε-Keggin core of molybdogermanate in extended architectures of nickel(II) with N-donor ligands: Syntheses, crystal structures and magnetic properties. *CrystEngComm* **2009**, *11*, 2488–2493. [CrossRef]
71. Reinoso, S.; Vitoria, P.; San Felices, L.; Montero, A.; Lezama, L.; Gutiérrez-Zorrilla, J.M. Tetrahydroxy-p-benzoquinone as a Source of Polydentate O-Donor Ligands. Synthesis, Crystal Structure, and Magnetic Properties of the [Cu(bpy)(dhmal)]2 Dimer and the Two-Dimensional $[\{SiW_{12}O_{40}\}\{Cu_2(bpy)_2(H_2O)(ox)\}_2]\cdot 16H_2O$ Inorganic−Metalorganic Hybrid. *Inorg. Chem.* **2007**, *46*, 1237–1249. [CrossRef]
72. Wu, X.-Y.; Zhang, Q.-K.; Kuang, X.-F.; Yang, W.; Yu, R.-M.; Lu, C.-Z. Two hybrid polyoxometalate-pillared metal–organic frameworks. *Dalton Trans.* **2012**, *41*, 11783–11787. [CrossRef] [PubMed]
73. Darling, K.; Smith, T.M.; Vargas, J.; O'Connor, C.J.; Zubieta, J. Polyoxometalate clusters as building blocks for oxide materials: Synthesis and structure of a three-dimensional copper-pyrazinetetrazolate/Keggin assembly. *Inorg. Chem. Commun.* **2013**, *32*, 1–4. [CrossRef]
74. Tripuramallu, B.K.; Das, S.K. Hydrothermal Synthesis and Structural Characterization of Metal Organophosphonate Oxide Materials: Role of Metal-Oxo Clusters in the Self Assembly of Metal Phosphonate Architectures. *Cryst. Growth Des.* **2013**, *13*, 2426–2434. [CrossRef]
75. Wang, X.-L.; Rong, X.; Liu, D.-N.; Lin, H.-Y.; Liu, G.-C.; Wang, X.; Song, G. Diverse polyoxometalate-based metal–organic complexes constructed by a tetrazole- and pyridyl-containing asymmetric amide ligand or its in situ transformed ligand. *CrystEngComm* **2016**, *18*, 5101–5109. [CrossRef]
76. Li, S.; Ma, H.; Pang, H.; Zhang, Z.; Yu, Y.; Liu, H.; Yu, T. Tuning the dimension of POM-based inorganic–organic hybrids from 3D self-penetrating framework to 1D poly-pendant chain via changing POM clusters and introducing secondary spacers. *CrystEngComm* **2014**, *16*, 2045–2055. [CrossRef]
77. Wang, D.-B.; Gao, H.; Bai, Y.; Hu, X.-F.; Yang, F.; Chen, Y.; Niu, J.-Y. A 2D helical coordination polymer based on Keggin-type polyoxoanion: Syntehesis, crysta structure and luminescent properties. *Inorg. Chem. Commun.* **2010**, *13*, 37–41. [CrossRef]
78. Han, Z.; Hao, Q.; Zhai, X.; Xie, J. Multiple supported Keggin-type polyoxometalate polymer built upon weak copper–oxygen interaction. *Inorg. Chim. Acta* **2012**, *382*, 105–110. [CrossRef]
79. Zhu, M.; Peng, J.; Pang, H.-J.; Zhang, P.-P.; Chen, Y.; Wang, D.-D.; Liu, M.-G.; Wang, Y.-H. Polyoxometalate immobilization in Cu^{I}/Ag–pz porous coordination polymers: The influences of them on the structural properties of frameworks. *J. Solid State Chem.* **2011**, *184*, 1070–1078. [CrossRef]
80. Wang, X.; Peng, J.; Alimaje, K.; Shi, Z.-Y. Keggin POM-based 3D framework tuned by silver polymeric motifs: Structural influences of tetrazolate functional groups. *CrystEngComm* **2012**, *14*, 8509–8514. [CrossRef]
81. Zhang, C.-H.; Zhang, C.-J.; Chen, Y.-G.; Liu, S.-X. A new 3D hybrid architecture containing Keggin-type tungstosilicate and $Cu_4(EGTA)_2$ metallamacrocyclic cation. *Inorg. Chem. Commun.* **2011**, *14*, 1465–1468. [CrossRef]
82. Zhang, C.-J.; Pang, H.-J.; Tang, Q.; Chen, Y.-G. A feasible route to approach 3D POM-based hybrids: Utilizing substituted or reduced Keggin anions with high charge density. *Dalton Trans.* **2012**, *41*, 9365–9372. [CrossRef] [PubMed]

83. Liu, H.-Y.; Wu, H.; Yang, J.; Liu, Y.-Y.; Ma, J.-F.; Bai, H.-Y. Solvothermal Assembly of a Series of Organic–Inorganic Hybrid Materials Constructed from Keggin Polyoxometalate Clusters and Copper(I)–Organic Frameworks. *Cryst. Growth Des.* **2011**, *11*, 1786–1797. [CrossRef]
84. Nakajima, K.; Eda, K.; Himeno, S. Effect of the Central Oxoanion Size on the Voltammetric Properties of Keggin-Type $[XW_{12}O_{40}]^{n-}$ (n = 2–6) Complexes. *Inorg. Chem.* **2010**, *49*, 5212–5215. [CrossRef]
85. Maeda, K.; Himeno, S.; Osakai, T.; Saito, A. A voltammetric study of Keggin-type heteropolymolybdate anions. *J. Electroanal. Chem.* **1994**, *364*, 149–154. [CrossRef]
86. Perdew, J.P.; Burke, K.; Ernzerhof, M. Generalized Gradient Approximation Made Simple. *Phys. Rev. Lett.* **1996**, *77*, 3865–3868. [CrossRef] [PubMed]
87. TURBOMOLE V6.4 2012, a Development of University of Karlsruhe and Forschungszentrum Karlsruhe GmbH, 1989–2007, TURBOMOLE GmbH, Since 2007. Available online: http://www.turbomole.com (accessed on 2 July 2021).
88. Christiansen, P.A.; Ermler, W.C.; Pitze, K.S. Relativistic Effects in Chemical Systems. *Annu. Rev. Phys. Chem.* **1985**, *36*, 407–432. [CrossRef]
89. Broyden, C.G. The Convergence of a Class of Double-rank Minimization Algorithms: 2. The New Algorithm. *J. Inst. Math. Appl.* **1970**, *6*, 222–231. [CrossRef]
90. Fletcher, R. A new approach to variable metric algorithms. *Comput. J.* **1970**, *13*, 317–322. [CrossRef]
91. Goldfarb, D. A family of variable-metric methods derived by variational means. *Math. Comput.* **1970**, *24*, 23–26. [CrossRef]
92. Shanno, D.F. Conditioning of quasi-Newton methods for function minimization. *Math. Comput.* **1970**, *24*, 647–656. [CrossRef]
93. Klamt, A.; Schüürmann, G. COSMO: A new approach to dielectric screening in solvents with explicit expressions for the screening energy and its gradient. *J. Chem. Soc. Perkin Trans.* **1993**, *2*, 799–805. [CrossRef]
94. Morokuma, K. Molecular Orbital Studies of Hydrogen Bonds. III. C=O···H–O Hydrogen Bond in $H_2CO···H_2O$ and $H_2CO···2H_2O$. *J. Chem. Phys.* **1971**, *55*, 1236. [CrossRef]
95. Ziegler, T.; Rauk, A. On the calculation of bonding energies by Hartree Fock Slater method. *Theor. Chim. Acta* **1977**, *46*, 1–10. [CrossRef]